JOURNAL OF GUIDANCE, CONTROL, AND DYNAMICS
Vol. 21, No. 5, September–October 1998

Control of Flexible Structures Using GPS: Methods and Experimental Results

E. Harrison Teague*
Seagull Technology, Inc., Los Gatos, California 95032
and
Jonathan P. How† and Bradford W. Parkinson‡
Stanford University, Stanford, California 94305

Active control of the attitude and vibration of a flexible structure using the Global Positioning System (GPS) is demonstrated. Measurements of the carrier phase of the GPS signal at several antennas are used to estimate the deformation and orientation of the structure. This distributed measurement capability, combined with excellent zero-frequency performance, makes the GPS sensor an excellent choice for a wide range of applications, including space structures, suspension bridges, and skyscrapers. The control system developed around the GPS sensor is presented for a particular structure modeled after the Space Station. The results from several new experiments demonstrate that the GPS sensor provides rotational accuracies better than 0.1 deg for static tests. Measured spectra also demonstrate that the carrier-phase GPS techniques are sufficiently accurate to resolve many of the modes of vibration. Several feedback control experiments are used to show that the sensor provides an accurate and robust measure of the structural deformations. These experiments culminate in a fast slew maneuver under feedback control, which provides a clear demonstration of the application of carrier-phase GPS for both alignment and vibration control. This work shows the potential for GPS as a high-precision, real-time structural sensor.

Nomenclature

A	= state-space system matrix
A_c, B_c	= continuous state-space system model matrices
B	= state-space forcing matrix
$\boldsymbol{B}$	= body frame
B_w	= state-space process noise matrix
b	= bias ambiguity
C	= diagonal modal damping matrix
C_i	= frame fixed to rigid body i
c	= clock offset
$\boldsymbol{h}(\cdot)$	= geometric measurement vector function
I	= identity matrix
J	= quadratic cost function
K	= loop gain matrix
$\boldsymbol{N}$	= lab fixed (Newtonian) frame
P	= covariance
$\boldsymbol{p}$, $\|p\|$	= position vector and its magnitude
Q_u	= control input weighting
Q_x	= state error weighting
q_i, $\boldsymbol{q}$	= generalized coordinates the vector of stacked coordinates
R, $\mathcal{R}$	= measurement noise weighting matrix
T	= sampling period
U	= mode matrix
$\boldsymbol{u}$	= vector of forcing terms
W, $\mathcal{W}$	= process noise weighting matrix
$\boldsymbol{w}$	= vector of process noise terms
X_1, $\mathcal{B}$	= initial state and bias weighting matrices
$\boldsymbol{x}$	= state vector
$\hat{\boldsymbol{x}}$	= current estimate of $\boldsymbol{x}$
$\Delta\phi$	= measured phase difference
δx	= estimate error
ζ	= damping coefficient
Λ	= diagonal modal frequency matrix
ν	= measurement noise
$\boldsymbol{\xi}$	= vector of modal coordinates
$\boldsymbol{\rho}$	= residual vector
Υ	= forcing matrix
τ_i	= time constant of mode i
Φ	= stiffness matrix
Ψ	= damping matrix
ψ	= phase polarization effects
ω_i	= frequency of mode i

Received Dec. 19, 1997; revision received April 28, 1998; accepted for publication April 29, 1998.

*Senior Project Engineer, 16400 Lark Avenue. Member AIAA.
†Assistant Professor, Department of Aeronautics and Astronautics. Member AIAA.
‡Professor, Department of Aeronautics and Astronautics. Fellow AIAA.

I. Introduction

THE presence of the L-band carrier waves broadcast by Global Positioning System (GPS) satellites enables a user to measure the relative position of antennas that are in close proximity to centimeter accuracy. This accuracy is based on the ability of current receivers to track the 19-cm carrier to a small fraction of the total wavelength.[1] The benefits of coupling precise GPS positioning and attitude determination to vehicle guidance and control already have been demonstrated for many land, marine, air, and space vehicles.[2–9]

Attitude determination is performed by comparing the differential carrier-phase measurements for an array of GPS antennas mounted on the vehicles. Achievable attitude accuracy is approximately inversely proportional to the baseline lengths (the distance between antennas).[1] Thus, it is advantageous to mount the antennas as far apart as possible to reduce the attitude errors induced by the measurement noise. However, many platforms of interest have nonnegligible elasticity, and increased baseline lengths amplify the antenna relative motion caused by platform vibrations. The detrimental effect of unmodeled platform elasticity was noted by van Graas and Braasch[3] in tests using a Douglas DC-3 aircraft (28-m wingspan) with wing-tip mounted antennas. Wing flexing during flight caused large measurement residuals, thereby increasing the estimate error and inhibiting measurement integrity checks.

To address the issue of platform flexibility, Cohen[4] and Cohen et al.[10] included a state variable to capture the wing flex in addition to the three attitude state variables. This wing flex state described the symmetric up-and-down bending of the wings in the body frame. In tests performed on a King Air 200, a 17-m-wingspan twin-turboprop aircraft, attitude accuracies of a few tenths of a degree were measured when compared to an onboard inertial navigation unit.[10] The

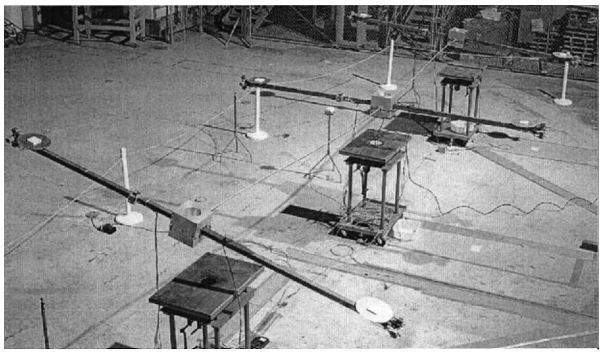

Fig. 1 Experimental structure in motion. The three center blocks are supported by suspension cables.

tests also showed wing flex magnitudes of ±7 cm from static flexure during rapid pitch maneuvers.

These initial aircraft test results suggested that carrier differential GPS (CDGPS) sensing could be used to measure the deformation of more general flexible platforms. For example, it should be possible to use CDGPS to measure the vibrations of structures, such as suspension bridges, skyscrapers, and oil rigs, that exhibit low-frequency, large-amplitude deformations. The research discussed in this paper focuses on demonstrating this technology for a space-based application. In particular, the goal was to develop the techniques necessary to use CDGPS to measure the orientation and deformation of a large orbiting space structure, such as the Space Station or the Shuttle robotic manipulator system (SRMS).

The applicability of GPS for sensing general platform vibrations is demonstrated with tests on an experimental flexible structure designed and built for this research (see Fig. 1). The test structure is an 8-m-long, 180-kg platform that is suspended from above in a large high-bay laboratory at Stanford. The structure has 10+ vibration modes (both bending and torsional) with frequencies below 0.5 Hz and it can rotate freely in the horizontal plane to enable tests of large-scale attitude slew maneuvers. Because the experiment is located indoors, the signals from the GPS satellites are not detectable. Therefore, a set of six pseudolite transmitters with custom transmit antennas was constructed and mounted on the ceiling and walls of the laboratory.[11] Note that the useful bandwidth of the sensing system is approximately from dc to 3 Hz (Nyquist at 5 Hz). The orientation and deformation of the structure can be controlled using a distributed array of air thrusters. This combination of sensing and control capabilities makes this facility quite unique when compared to the vast number of experimental test beds that have been developed to study the control of flexible structures on the ground[12,13] and in space.[14]

The main goal is to demonstrate the feasibility of simultaneously estimating the deformation and overall attitude of a prototypical space structure using carrier measurements from a distributed array of antennas. Proof-of-concept experiments were performed by Teague and Parkinson[15] to show the estimation of the modal deflections of a one-dimensional beam. Previous research is extended by generalizing the CDGPS sensing to structures that exhibit many three-dimensional flexible modes in addition to rigid-body attitude degrees of freedom. The results show that the modal behavior can be estimated, with sufficient accuracy for feedback control, in real time using an extended Kalman filter. With six GPS antennas, 24 thrusters, and a complicated flexible structure, one of the most advanced closed-loop control experiments that has been demonstrated using CDGPS as the only sensor is presented.

A key step in this research was to demonstrate how to extend previously used kinematic ambiguity initialization algorithms and point solution state estimators[3–6] to incorporate a dynamic model of the structure to enhance the state estimates. The importance of the dynamic approach to ambiguity initialization for flexible structures is presented in detail in Refs. 16 and 17. However, Ref. 17 focuses primarily on the sensing and actuator hardware on the structure and on the analysis of the various initialization problems for the GPS sensor.

The results in Ref. 17 are extended in several key ways. First, a more comprehensive discussion of the GPS-based control system is provided, including detailed analysis of the structural model and the full-state feedback regulator. The real-time nonlinear extended Kalman filter that is required to estimate large-angle attitude slews also is discussed in some detail. The estimator is closely coupled with the GPS sensor and is the main component of the feedback control system. We also present the results of several new experiments that clearly demonstrate the excellent static and dynamic performance of the GPS sensor. Furthermore, several feedback control experiments are used to show that the sensor provides an accurate and robust measure of the structural deformations. These new experiments culminate in a very fast slew maneuver under feedback control, which provides a clear demonstration of the application of carrier-phase GPS for both alignment and vibration control.

All sensing systems are plagued with a variety of measurement errors that limit the achievable accuracy and performance. The dominant error in most CDGPS sensors is due to multipath, which results in an antenna positioning error of approximately 1.5 cm (1σ) for this test bed. A further problem with CDGPS is that the measurements from an antenna array with nonaligned boresights are corrupted by the circular polarization of the signal.[11,18] A third key problem with CDGPS sensors in space applications is that the GPS satellites are very rapidly lost and acquired, which greatly complicates the recursive filter and initialization algorithm logistics. The multipath errors limit the achievable pointing accuracy for this structure, but the other two errors do not significantly affect the experimental results. These errors would be critical for more realistic applications, and many researchers are investigating techniques to reduce their effects.[18–22] Although the experiments have been performed indoors on the ground, the GPS receivers already have been qualified for and demonstrated in space.[8,22] Thus the technologies presented herein easily could be tested on-orbit.

The error sources mentioned earlier make the accuracy of a CDGPS sensor insufficient for control of a platform with fine-pointing control requirements, such as the Hubble Space Telescope. However, this CDGPS technology could be valuable for outer-loop attitude and vibration control of a platform to enhance the performance of a localized fine-pointing subsystem.

This technology may be applied directly to other flexible structures that vibrate with dominant frequencies between dc and 5 Hz. Terrestrial structures such as bridges and buildings could use the sensor for nondestructive evaluation of structural integrity and, in the presence of actuators, for real-time control. The remainder of this paper describes the estimation and closed-loop control results demonstrated on our flexible structure.

II. CDGPS Measurement

Although many test facilities have been developed to demonstrate active vibration control, the test bed used for these experiments is unique because the structural vibrations are sensed using very precise GPS measurements. The following section presents the general differential carrier phase observable with all terms included. The expressions then are simplified using the assumptions made for the flexible structure experiment. A CDGPS measurement consists of the difference in the line-of-sight distance from a transmitter to a pair of antennas, plus a bias, plus a clock offset, plus phase polarization effects, plus noise.[9] The CDGPS observable can be written (in units of length) as

$$\Delta\phi_{lij} = |\boldsymbol{p}_{ji}| - |\boldsymbol{p}_{jl}| + b_{lij} + c_{li} + \psi_{lij} + \nu_{lij} \tag{1}$$

where

$\Delta\phi_{lij}$ = the CDGPS carrier phase observable from antennas l and i, which uses the signal from transmitter j.

$|\boldsymbol{p}_{ji}| - |\boldsymbol{p}_{jl}|$ = the difference in the position vector magnitudes, which is the primary geometric information in the measurement. This term is only a function of the transmitter and antenna positions; $\boldsymbol{p}_{ji}$ is the position vector from transmitter j to antenna i.

b_{lij} = the bias term, which accounts for the unknown offset of the measurement at the time of signal lock at both antennas. This term includes differences in the electrical length (antenna to the receiver correlator) for the two antennas (line bias), and the ambiguous number of full cycles in the initial measurement (cycle ambiguity). Because the line bias is only hardware dependent, it can be calibrated a priori for a particular hardware configuration.

c_{li} = the clock bias, which is the difference in the clock reference for phase measurements between the two antennas. Because a carrier wave travels 300 km/ms, this term must be minimized in hardware or eliminated using multiple measurements.

ψ_{lij} = phase polarization effects, which are deviations in the phase measurement due to angle of signal incidence on antennas. This effect has been negligible in the past because most applications have used the antennas that have common boresight directions, where the effect cancels. A detailed analysis of this effect is given by Zimmerman.[11]

ν_{lij} = the noise term, which encompasses all other unmodeled effects (such as multipath) and receiver noise.

For the flexible-structure research project, an array of six antennas was mounted on the test structure and connected to two four-antenna receivers. The antenna multiplexing design of the receivers allows phase differencing relative to a common clock signal, eliminating clock bias errors c_{il}. For systems in which a common clock signal is not possible, double differencing between two signal sources can be used to remove the clock offset.[3]

Because of the orientation and alignment of the antennas on the test structure, and because antenna relative attitude motion has a limited magnitude for our experiments, phase polarization effects ψ_{ijl} are assumed to be small.[16] For applications in which the relative antenna attitude is not small, or is unconstrained, this effect should be included.[18,21]

Neglecting the clock offset and phase polarization effects, and using the common master antenna architecture, Eq. (1) can be simplified to

$$\Delta\phi_{ij} = |\boldsymbol{p}_{ji}| - |\boldsymbol{p}_{jM}| + b_{ij} + \nu_{ij} \tag{2}$$

Note that the l index has been dropped because of the common master configuration. The M index in the second position vector magnitude denotes the master antenna.

The CDGPS measurement for a single transmitter and baseline is illustrated (without bias b_{ij}) in Fig. 2, which shows traveling GPS wavefronts as circular arcs. It is common to assume that the wavefronts from the very distant GPS satellites are planar, thereby simplifying the measurement equation. However, GPS signals generated by nearby pseudolites are not well approximated as planar. Pseudolites also have been used for many other applications to replace or augment the satellite constellation.[11,23,24] Because a near constellation of pseudolites was used for this work, the planar wavefront assumption was not used.

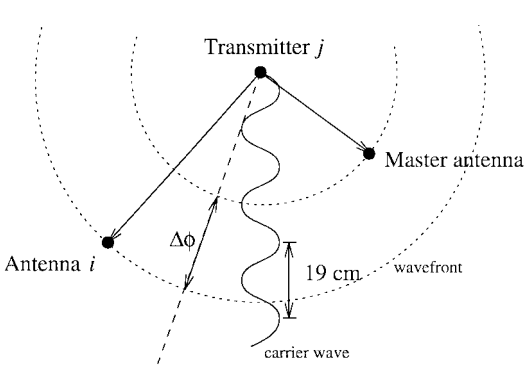

Fig. 2 Carrier differential GPS measurement.

For notational convenience, $\Delta\phi_{ij}$, b_{ij}, and ν_{ij} can be stacked for all i and j to form single vectors denoted $\boldsymbol{\Delta\Phi}$, $\boldsymbol{b}$, and $\boldsymbol{\nu}$ respectively. The vector measurement equation then is written as

$$\boldsymbol{\Delta\Phi} = \boldsymbol{h}(\boldsymbol{x}) + \boldsymbol{b} + \boldsymbol{\nu} \tag{3}$$

where $\boldsymbol{x}$ is the state vector for the system. Equation (3) is written in a form that is quite standard for most CDGPS problems. However, as discussed in Sec. IV, the solution in this case requires a model of the flexible structure, the derivation of which is presented in Sec. III.

III. System Modeling

A. Experimental Test Structure

To develop and test the GPS sensing system for flexible structures, an experimental facility was constructed with several important characteristics in mind. In particular, a test bed was built to emulate the motion of a large, flexible, orbiting platform that vibrates with low-frequency modes and large structural deflections. Although the test structure was designed to produce motion of onboard antennas that is characteristic of points on a large flexible structure (slow motion with very low damping), the model is not intended to duplicate the dynamics of any particular space platform. The test structure is suspended from an overhead crane in a large high-bay (20-m tall) facility at Stanford, and it is outfitted with sensors and actuators for real-time control experiments. The structure was designed to have the following key characteristics:

1) Large elastic deformations with low damping. Because a major goal of this work is to study the effect of nonnegligible structural elasticity on GPS motion sensing, large elastic deformations are required. The low damping in the structure accentuates the need for active vibration control.

2) Antenna motions detectable by GPS. During system deformation, the antennas must undergo motions that are detectable by GPS receivers. The carrier phase tracking loops in the receivers used for this work have a bandwidth of approximately 10 Hz and they can detect antenna motions of approximately 1 cm or greater. Motions of a typical flexible orbiting platform are well within these sensor limits.

3) Simultaneous elastic and orientation motion. A second major goal of this work is to demonstrate simultaneous control of vibrations and overall pointing of the structure using GPS as the sole source of flex motion and overall attitude information.

The structure is an assembly made primarily of aluminum and steel that hangs by 12-m threads from an overhead crane. This assembly comprises three massive and essentially rigid sections that are connected in a horizontal line by long elastic beams with endpoints that are fixed to the rigid sections (see Fig. 3). This configuration, with massive rigid sections connected by light elastic beams, provides the low frequencies needed by simultaneously achieving high mass and high elasticity. Each rigid section consists of a 25-cm aluminum cube with two iron arms that are rigidly attached to the cube and extend outward in the horizontal plane. The endpoints of the arms provide the mounting points for the antennas and actuators. The elastic beams between the cubes are $\frac{1}{2}$-in.-diam, thin-walled aluminum tubes that bend and twist during motion of the entire system. Although the beams are very flexible and long (3.7 m), they sag by only 1–2 cm at their midpoints because of gravity.

Each thread of the suspension system is attached to one of the rigid sections of the assembly just above its center of mass. This suspension technique reduces the frequency of the suspension-induced pendulum modes and allows the entire system to move like a structure in a zero-gravity environment, with low frequencies and low damping. Balancing the structure after full assembly is required and can be performed using mechanisms that allow millimeter-level adjustments, in three dimensions, of the point of attachment of the suspension thread to the rigid section. Finally, to allow overall orientation changes of the structure, the suspension threads are attached at the top to a rigid beam that is mounted to a thrust bearing, allowing the beam and the structure below to rotate freely in the horizontal plane. This rigid-body mode allows experiments in both structural pointing control and slew maneuvers.

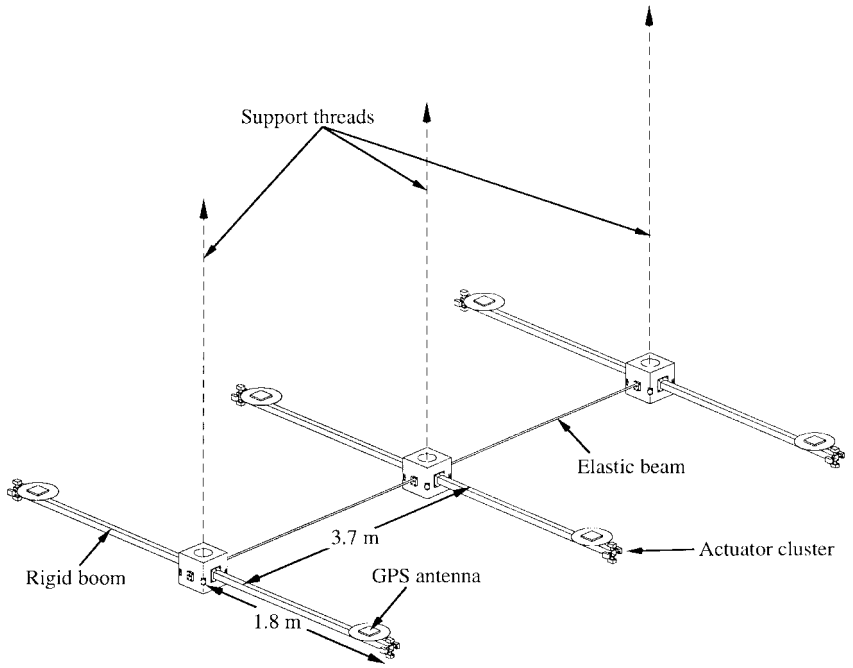

Fig. 3 Test structure (see Fig. 1).

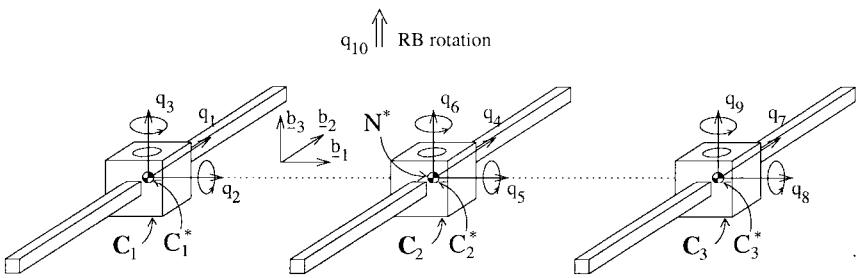

Fig. 4 Definition of the generalized coordinates for the structural model.

A system of 24 on/off gas thrusters is used to impart forces on the test structure. These thrusters are used for control actuation and for disturbance input in the control experimentation described. As shown in Fig. 3, a cluster of four actuators is located on the end of each of the six rigid booms. The thruster configuration (location and orientation) was chosen to provide control of all important modes of structural motion.

In addition to the GPS sensors, six inexpensive, single-axis, rate gyroscopes were mounted on the test structure, primarily to provide an independent measurement with which to compare the GPS results. The gyros are mounted to the arms of the rigid sections, three on the center section, two on one of the outer sections, and one on the third section. Orientation of a rigid section can be found by simply integrating the signals from the gyroscopes. A calibration of the gyros was performed to find the gyro offsets and to minimize inherent drift errors from these inertial sensors. However, even with calibration prior to each experimental session, the gyro drift is non-negligible, even for the relatively short-duration experiments (1–2 min). This points out an important advantage to GPS sensing over inertial sensing: dc performance. The GPS and gyroscope measurements are compared in Sec. VI.

The configuration of the structure is described in terms of 10 generalized coordinates, q_1–q_{10}. Coordinates q_1–q_9 describe the elastic deformation of the structure relative to a body frame, $\boldsymbol{B}$. In particular, the coordinates describe translations and rotations of the three rigid sections (denoted $\boldsymbol{C}_1$, $\boldsymbol{C}_2$, and $\boldsymbol{C}_3$) as shown in Fig. 4. Although six coordinates are required to define the general motion of a rigid body, only three were needed for this system. The additional degrees of freedom, e.g., translation in the $\underline{b}_1$ and $\underline{b}_3$ directions, are not critical for typical motions of the structure, and, for the sake of computational efficiency, were not included in the model. The primary modes of motion that are included in the final model (see Fig. 5 and Table 1) do not require these additional parameters and are specified completely by q_1–q_9. The rigid-body angle q_{10} describes the rotation of frame $\boldsymbol{B}$ about a vertical axis in the laboratory fixed frame $\boldsymbol{N}$. The choice of the $\boldsymbol{B}$ frame is theoretically arbitrary. There are, however, significant computational advantages to using a frame about which the elastic motions are small because the measurement equations then can be linearized. For this research, the specification of the orientation of the $\boldsymbol{B}$ frame (q_{10}) is an output of the recursive extended Kalman filter (described in Sec. IV).

B. Equations of Motion

The equations of motions for flexible structures have been well documented in the literature, and so, this section only provides a brief overview of the techniques used to derive a model of the flexible structure in discrete state-space form

$$\boldsymbol{x}_{k+1} = A\boldsymbol{x}_k + B\boldsymbol{u}_k + B_w\boldsymbol{w}_k \tag{4}$$

The standard second-order linear differential equation describing the variation of the physical coordinates $\boldsymbol{q}$ with time can be written as

$$\ddot{\boldsymbol{q}} + \Psi\dot{\boldsymbol{q}} + \Phi\boldsymbol{q} = \Upsilon\boldsymbol{u} \tag{5}$$

This equation relies on the assumption that the first and second derivatives of the nonlinear coordinate q_{10} are well approximated as small. Hence, the equations are linear in q_{10} and any coupling (centrifugal stiffening) between the rigid-body motion (q_{10}) and the elastic motion (q_1–q_9) can be neglected. These assumptions are valid for this system because the rigid-body slew rates are typically quite small (<3 deg/s). The minimum slew rates for this assumption to

Table 1 Characteristics of structural model.

Mode[a]	Description	Mode frequency,[b] Hz	Time constant τ, s	Damping ratio, $\zeta = 1/w\tau$
1	Pendulum mode	0.059	20	0.134
2	Swing mode	0.160	130	0.007
3	First bending mode	0.132	200	0.006
4	First twist mode	0.085	45	0.042
5	Second twist mode	0.138	35	0.033
6	Second bending mode	0.135	140	0.008
7	Third bending mode	0.23	50	0.014
8	Fourth bending mode	0.28	25	0.023
9	Rigid-body mode	0.0	140	——

[a]Mode numbers correspond to Fig. 5.
[b]Mode frequencies were measured experimentally and are accurate to within 5%.

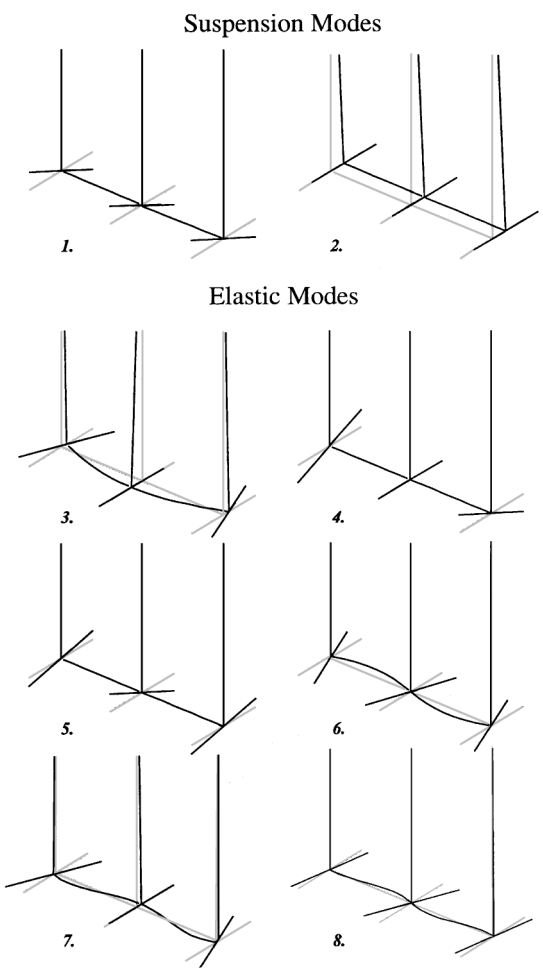

Fig. 5 Primary flexible modes of the structure. Deformations are exaggerated for effect. The mode frequencies and names are given in Table 1.

hold on a real orbiting platform depend on the mass properties of the particular platform.

It is convenient to decouple these equations using the modal transformation matrix U, where $\boldsymbol{q} = U\boldsymbol{\xi}$. Define the diagonal matrix $\Lambda = U^T\boldsymbol{\Phi}U = \text{diag}(\omega_i^2)$ and assume that U also diagonalizes $C = U^T\Psi U = \text{diag}(-2\zeta_i\omega_i)$ (standard modal damping assumption). We then can rewrite the equations of motion as $\ddot{\boldsymbol{\xi}} + C\dot{\boldsymbol{\xi}} + \Lambda\boldsymbol{\xi} = U^T\Upsilon\boldsymbol{u}$, or with $\boldsymbol{x} = [\boldsymbol{\xi}^T \;\; \dot{\boldsymbol{\xi}}^T]^T$

$$\dot{\boldsymbol{x}} = A_c\boldsymbol{x} + B_c\boldsymbol{u} \tag{6}$$

where

$$A_c = \begin{bmatrix} 0 & I \\ -\Lambda & -C \end{bmatrix}, \qquad B_c = \begin{bmatrix} 0 \\ U^T\Upsilon \end{bmatrix} \tag{7}$$

The c subscript denotes a continuous model matrix that can be discretized using the zero-order-hold approximation on the inputs[25] and sampling period T.

The mode shapes U were determined using MSC/NASTRAN computing facilities at NASA Ames Research Center. Only the nine lowest frequency modes were retained in the final model, including the eight elastic modes shown in Fig. 5 and a rigid-body mode describing the rotation of the entire assembly in the horizontal plane. These nine modes dominate the system response and provide a very good approximation of the motion corresponding to the physical coordinates $\boldsymbol{q}$. As is commonly done for approximate system modeling of this type, the analytically determined mode frequencies and damping coefficients (Λ and C) were adjusted to better fit the experimental measurements from free-response tests on the actual system. The final values used are given in Table 1.

The next step was to determine a force model that describes how the thruster forces should be included in the equations of motion. The end result of this analysis is the matrix B in Eq. (4), which essentially reduces to finding Υ in Eq. (5). This was accomplished by independently writing a set of force and moment equations for the actuators on each of the rigid sections. An equation for the entire assembly angular velocity also was analyzed to include the rigid-body rotation degree of freedom. These equations were linearized and expressed in the simple matrix form $\ddot{\boldsymbol{q}} = \Upsilon\boldsymbol{u}$, where $\boldsymbol{q}$ is the vector of generalized coordinates. This is a straightforward, but extremely complex, algebraic process, and so, all manipulations, including linearization of the equations, were performed by the symbolic manipulator program Autolev®.

A model of process noise is an important part of the real-time recursive estimator and the sensor initialization. The primary goal of the process noise model is to affect the relative weighting between the model and the measurements in optimal state (and bias) estimators. However, because there is really no significant process noise for the experimental system (such as vibration or wind), we follow the standard procedure of adding a fictitious process noise model. In particular, we add white process noise to each modal acceleration, so that in Eq. (4), $B_w^T = [0^T \;\; I^T]$. Because the process noise is fictitious, the covariance of the white noise $\boldsymbol{w}_k$ is difficult to assign a priori. Several covariance values were tried, and for the experiments in this paper, the process noise covariance $W = E[\boldsymbol{w}_k\boldsymbol{w}_k^T] = \text{diag}(0.5^2, \ldots, 0.5^2, 0.05^2)$ gave the best results (fast response with small overshoot).

This completes the formulation of the forced dynamic model in Eq. (4). The equations are formulated by inserting Λ, C, Υ, and U (columns are the modes in Fig. 5) into Eq. (7) and discretizing at 10 Hz ($T = 0.1$ s) to give the final A and B matrices in Eq. (4). The process noise model is added as described above. Of course, further model studies using I/O system identification also could be used for this system. However, this analytic model was sufficiently accurate for the real-time estimation and control experiments in this paper. A more detailed description of the system modeling is provided in Ref. 16.

IV. Measurement Processing

In this section, we combine the differential carrier-phase measurement with the dynamic model of the system and present the techniques needed to estimate the system response in real time. Given knowledge of the pseudolite phase center locations and the position of the antennas on the experimental structure, the position vectors, $\boldsymbol{p}_{ji}$ in Eq. (2) can be written in terms of the state $\boldsymbol{x}_k$ only.[16] The subscript k is a time (or epoch) index. The goal of the measurement processing algorithm is to estimate $\boldsymbol{x}$ in Eq. (3), repeated here for epoch k for convenience:

$$\Delta\boldsymbol{\Phi}_k = \boldsymbol{h}(\boldsymbol{x}_k) + \boldsymbol{b} + \boldsymbol{\nu}_k \tag{8}$$

Unfortunately, because each measurement is corrupted by a constant bias, a solution for $\boldsymbol{x}$ is not possible until an estimate of the biases is available. Thus, the measurement processing is split into two parts:

1) Perform a bias initialization routine to find an accurate estimate of $\boldsymbol{b}$.

2) Execute an estimator that uses the initialized biases to find estimates of $\boldsymbol{x}_k$ in real time.

A. Bias Initialization

Given that the biases are fixed in time, it is possible to use measurements taken during dynamic geometric motion of the flexible structure and a model of the structure's dynamics to determine the biases. A detailed analysis of the difficulties associated with using standard bias initialization techniques on a system with flexibility is given in Refs. 16 and 17. As a result, a new technique was developed for this research, using a batch nonlinear dynamic least-squares estimator. For this work, initialization was performed on the unforced system (free motion), and so, the effects of forcing [$\boldsymbol{u}_k$ in Eq. (4)] were not included.

The first step in this algorithm is to linearize Eq. (8) about the current best guess of the state $\hat{\boldsymbol{x}}_k$ and biases $\hat{\boldsymbol{b}}$, where $\boldsymbol{x}_k = \hat{\boldsymbol{x}}_k + \delta\boldsymbol{x}_k$ and $\boldsymbol{b} = \hat{\boldsymbol{b}} + \delta\boldsymbol{b}$. Assuming that the perturbations $\delta\boldsymbol{b}$ and $\delta\boldsymbol{x}_k$ are small, Eq. (8) can be rewritten as

$$\boldsymbol{\rho}_k = \Delta\boldsymbol{\Phi}_k - \boldsymbol{h}(\hat{\boldsymbol{x}}_k) - \hat{\boldsymbol{b}} = H(\hat{\boldsymbol{x}}_k)\delta\boldsymbol{x}_k + \delta\boldsymbol{b} + \boldsymbol{\nu} \tag{9}$$

where the linearized measurement equation is given by

$$H_k = H(\hat{\boldsymbol{x}}_k) = \left.\frac{\partial \boldsymbol{h}}{\partial \boldsymbol{x}_k}\right|_{x_k = \hat{x}_k} \tag{10}$$

Writing the perturbation form of Eq. (4) (assuming zero control forces for the initial motion) as

$$\delta\boldsymbol{x}_k = A\delta\boldsymbol{x}_{k-1} + B_w\boldsymbol{w}_{k-1} \tag{11}$$

$$= A^{k-1}\delta\boldsymbol{x}_1 + \sum_{i=1}^{k-1} A^{k-i-1}B_w\boldsymbol{w}_i \tag{12}$$

the entire linearized set of equations for N epochs then can be written as

$$\left[\begin{array}{c}\boldsymbol{\rho}_1\\ \boldsymbol{\rho}_2\\ \vdots\\ \boldsymbol{\rho}_N\\ \hline \mathbf{0}\\ \mathbf{0}\\ \vdots\\ \mathbf{0}\end{array}\right] = \left[\begin{array}{cccccc} H_1 & 0 & 0 & & 0 & I\\ H_2A & H_2B_w & 0 & & 0 & I\\ H_3A^2 & H_3AB_w & H_3B_w & \cdots & 0 & I\\ H_4A^3 & H_4A^2B_w & H_4AB_w & & 0 & I\\ & \vdots & & \ddots & \vdots & \vdots\\ H_NA^{N-1} & H_NA^{N-2}B_w & H_NA^{N-3}B_w & \cdots & H_NB_w & I\\ \hline \multicolumn{6}{c}{I}\end{array}\right]\left[\begin{array}{c}\delta\boldsymbol{x}_1\\ \boldsymbol{w}_1\\ \boldsymbol{w}_2\\ \vdots\\ \boldsymbol{w}_{N-1}\\ \delta\boldsymbol{b}\end{array}\right] + \boldsymbol{\nu} \tag{13}$$

or, for compactness,

$$\left[\begin{array}{c}\boldsymbol{\rho}\\ \hline \mathbf{0}\end{array}\right] = \left[\begin{array}{c}\Theta\\ \hline I\end{array}\right]\left[\begin{array}{c}\delta\boldsymbol{x}_1\\ \boldsymbol{w}\\ \delta\boldsymbol{b}\end{array}\right] + \boldsymbol{\nu} \tag{14}$$

The identity partition allows for the inclusion of estimated process noise covariance in the weighted least-squares solution. The iterative procedure for computing the batch solution is as follows:

1) Collect and store measurements at N equally spaced epochs as the physical system is in motion.

2) Define the diagonal weighting matrix $W = E[\boldsymbol{w}_k\boldsymbol{w}_k^T]$ as the best estimate of the process noise covariance. Also, define $R = E[\boldsymbol{\nu}_k\boldsymbol{\nu}_k^T]$ as the best estimate of the white measurement noise covariance. Then, let $\mathcal{W}$ equal the block diagonal concatenation of $N-1$ W matrices and $\mathcal{R}$ equal the block diagonal concatenation of N R matrices.

3) Define the diagonal weighting matrices, $\mathcal{B}^{-1}$ and X_1^{-1}. These determine the relative weighting of the $\delta\boldsymbol{b}$ and $\delta\boldsymbol{x}_1$ portions of the state, and nonzero values limit the magnitude of $\boldsymbol{b}$ and $\boldsymbol{x}_1$ updates per iteration. They may be set to zero or scaled to improve convergence of the batch estimator.

4) Perform the batch solution by iterating Eq. (15) until convergence:

$$\left[\begin{array}{c}\delta\hat{\boldsymbol{x}}_1\\ \hat{\boldsymbol{w}}\\ \delta\hat{\boldsymbol{b}}\end{array}\right] = \left(\Theta^T\mathcal{R}^{-1}\Theta + \left[\begin{array}{ccc} X_1^{-1} & & \\ & \mathcal{W}^{-1} & \\ & & \mathcal{B}^{-1}\end{array}\right]\right)^{-1}\Theta^T\mathcal{R}^{-1}\boldsymbol{\rho} \tag{15}$$

The iteration starts with an initial guess of $\hat{\boldsymbol{x}}_1$, $\hat{\boldsymbol{b}}$, and $\hat{\boldsymbol{w}}$. The next step is to use this guess to compute $\boldsymbol{x}_k$, $k = 2, \ldots, N$ from Eq. (4). Next, compute $\boldsymbol{\rho}$ and Θ from Eqs. (9), (10), (13), and (14), and use Eq. (15) to compute a new guess of $\hat{\boldsymbol{w}}$ and to refine the state and bias guesses using $\hat{\boldsymbol{x}}_1^{\text{new}} = \hat{\boldsymbol{x}}_1^{\text{old}} + \delta\hat{\boldsymbol{x}}_1$ and $\hat{\boldsymbol{b}}^{\text{new}} = \hat{\boldsymbol{b}}^{\text{old}} + \delta\hat{\boldsymbol{b}}$. An iterative algorithm is required because of the nonlinearity in the measurement equation (Θ is a function of the state estimate).

This technique was used to compute measurement biases to centimeter-level accuracy for the experimental results given in this paper.[16] Convergence typically requires 1–2 min for the flexible structure system on a Pentium® 120.

B. Real-Time State Estimation

The second main component of the measurement processing for this research is the real-time state estimator. The recursive real-time estimator is based on the discrete extended Kalman filter (EKF).[26] The EKF consists of two steps. A time update followed by a measurement update [the symbol $\bar{(\cdot)}$ denotes intermediate quantities between the time and measurement updates] is implemented as follows:

Given the model of Eq. (4)

$$\boldsymbol{x}_0 = \text{initial condition guess}$$

$$\boldsymbol{b} = \text{bias ambiguity estimate}$$

$$W = E\left[w_k w_k^T\right] \tag{16}$$

$$R = E\left[\boldsymbol{\nu}_k\boldsymbol{\nu}_k^T\right] \tag{17}$$

Time Update

$$\bar{\boldsymbol{x}}_k = A\boldsymbol{x}_{k-1} + B\boldsymbol{u}_{k-1} \tag{18}$$

$$\bar{P}_k = AP_{k-1}A^T + B_wWB_w^T \tag{19}$$

Measurement Update

$$P_k = \bar{P}_k - \bar{P}_k H_k^T \left[H_k \bar{P}_k H_k^T + R \right]^{-1} H_k \bar{P}_k^T \tag{20}$$

$$\boldsymbol{\rho}_k = \Delta \boldsymbol{\Phi}_k - \boldsymbol{h}(\bar{\boldsymbol{x}}_k) - \boldsymbol{b} \tag{21}$$

$$K = P_k H_k^T R^{-1} \tag{22}$$

$$\boldsymbol{x}_k = \bar{\boldsymbol{x}}_k + K \boldsymbol{\rho}_k \tag{23}$$

where H_k is given by Eq. (10). Then, given the solution to the batch bias initialization, these equations are propagated forward in time to give estimates for the state of the system, which includes the rigid-body and flexible modes. For typical sensor noise values [equivalent to 2 cm (1 σ) uncertainty in the antenna position] and the fictitious process noise added, this EKF converged within 0.5–1 s.

V. Control

To complete the control system, we also must design a regulator to feed back the estimated state $\hat{\boldsymbol{x}}_k$ and control the structural vibrations. A variety of techniques are available to design full-state feedback regulators but one of the simplest is the linear quadratic regulator (LQR), which minimizes the cost function

$$J = \sum_{k=0}^{\infty} \boldsymbol{x}_k^T \boldsymbol{Q}_x \boldsymbol{x}_k + \boldsymbol{u}_k^T \boldsymbol{Q}_u \boldsymbol{u}_k \tag{24}$$

where $\boldsymbol{x}$ is a vector of 18 state variables and $\boldsymbol{u}$ is a vector of 24 actuator commands for the flexible structure system. The solution for the LQR control gains is well known[27] and need not be discussed. The weights ($\boldsymbol{Q}_x$ and $\boldsymbol{Q}_u$) were tuned by analyzing the control performance on simulated data to determine the maximum control authority that could be applied without saturating the actuators. This led to the selection of

$$\boldsymbol{Q}_x^{\star} = 5000\,\mathrm{diag}(1, 1, 1, 1, 1, 1, 1, 1, 0.01)$$

$$\boldsymbol{Q}_x = \mathrm{diag}\left(\boldsymbol{Q}_x^{\star}, 0.01\,\boldsymbol{Q}_x^{\star}\right), \qquad \boldsymbol{Q}_u = I$$

An analysis of the system equations yields the open- and closed-loop poles shown in the z plane (first quadrant) in Fig. 6. The open-loop poles are shown as $\times$ and the closed-loop poles as $+$. The single closed-loop pole that is closest to $z = 1$ corresponds to the rigid-body motion and has a settling time of approximately 30 s. The other closed-loop poles correspond to vibration modes and have settling times of approximately 5 s, which is much faster than the open-loop values in Table 1. The main limitation to the control performance in this system is the 1.4-N maximum thrust of the gas jet actuators.

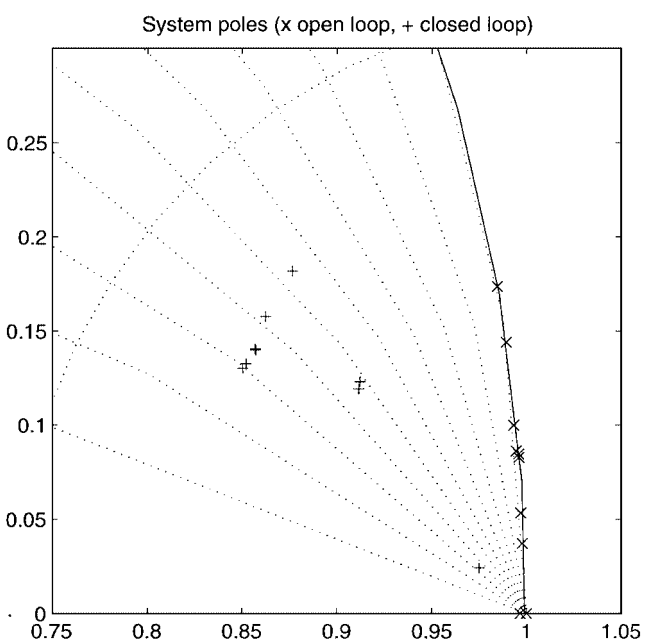

Fig. 6 Pole locations.

This limits the extent to which the closed-loop poles can be moved to more highly damped regions of the z plane in Fig. 6.

The real-time system hardware consists of a 200-MHz computer running a real-time operating system. The computer reads GPS data, computes system state estimates and control commands, and issues thruster commands at 10 Hz. The control commands are realized using a pulse-width pulse-frequency modulation transformation to the on/off thrusters. See Ref. 16 for a more complete description of the control formulation, including weight assignment and control simulations.

VI. Experimental Results

This section presents several tests of the control system described in the preceding section when connected to the physical system. The section is separated into two tests of the GPS sensor and three closed-loop control experiments. The results clearly illustrate that CDGPS can be used to sense and control the alignment and vibrations of a flexible structure.

A. Static Sensor Tests

The first test was performed to show that CDGPS measurements provide a very accurate, drift-free measure of the static alignment of the structure. The first step in this experiment was to perform the bias initialization. The structure then was allowed to come completely to rest at approximately 0-deg rigid-body angle (plus or minus a couple of degrees). For convenience, let the center section vertical (CSV) angle denote $q_6 + q_{10}$ as shown in Fig. 4. A laser optical survey of the rest position very accurately determined the CSV angle to be -1.4 deg. Data from GPS and gyro sensors were collected and the resulting estimates of the CSV angle from GPS and gyro estimates are plotted in Fig. 7. The top plot shows the GPS and gyro estimates and the bottom plot shows their difference. The GPS estimator predicts the CSV angle to be approximately -1.48 deg with essentially no drift and an estimated noise of less than 0.02 deg rms. The gyro estimate, initialized by the GPS estimate, has comparable noise magnitudes but has a noticeable drift over time that is consistent with the manufacturer's specifications.

The extremely low GPS estimate noise in this case is due to the low measurement noise for static tests (about 2 mm rms for this test) and the highly redundant measurement set (36 measurements and 18 states). These results show an excellent agreement (to within a tenth of a degree) between the GPS estimates and the laser survey. This result also confirms the validity of the bias estimate computed prior to the static test because the bias estimate fixes the absolute rigid-body degree of freedom in the laboratory frame.

B. Dynamic Sensor Test

The next test is an evaluation of the sensor performance during dynamic system motion. First, the structure was lifted from its support tables and balanced. Then, random excitation was manually applied in an attempt to introduce energy into the primary system vibration modes (the author physically maneuvered the structure at various locations until a "random" vibration was generated). CDGPS data and rate gyroscope data were taken during this random free motion of the flexible structure. To analyze the sensor data and to compare the GPS and gyroscope information, the power spectral density was computed for both sets of sensor data. Figure 8 shows a comparison of these two spectra. The gyroscope spectrum is divided by frequency to allow a one-to-one frequency-domain comparison of its rate measurements with the position measurements from GPS. Modal behavior is shown by the clear resonance peaks, and the agreement of the peak frequencies between the GPS and gyroscope data is apparent. The peak frequencies in Fig. 8 are within 5% of the frequencies used for the final model of Table 1. Differences in the spectral magnitudes between the two sensors illuminate their different observability characteristics. A notable contrast is the lack of low-frequency modes in the gyroscope data. This could be caused by the poor low-frequency performance of the imperfect inertial sensor or by the unobservability of some modes, such as modes involving predominantly rigid-body translation, from rate gyroscope measurements.

Together, these static and dynamic sensor results demonstrate that CDGPS provides a drift-free measure of the low-frequency motion of the structure and that the CDGPS techniques are sufficiently

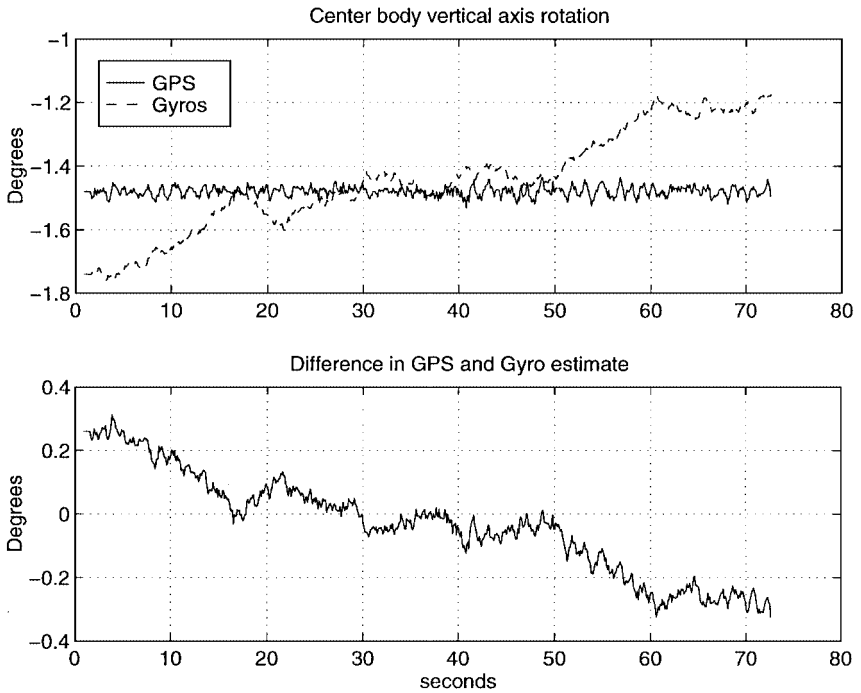

Fig. 7 Static estimator comparison.

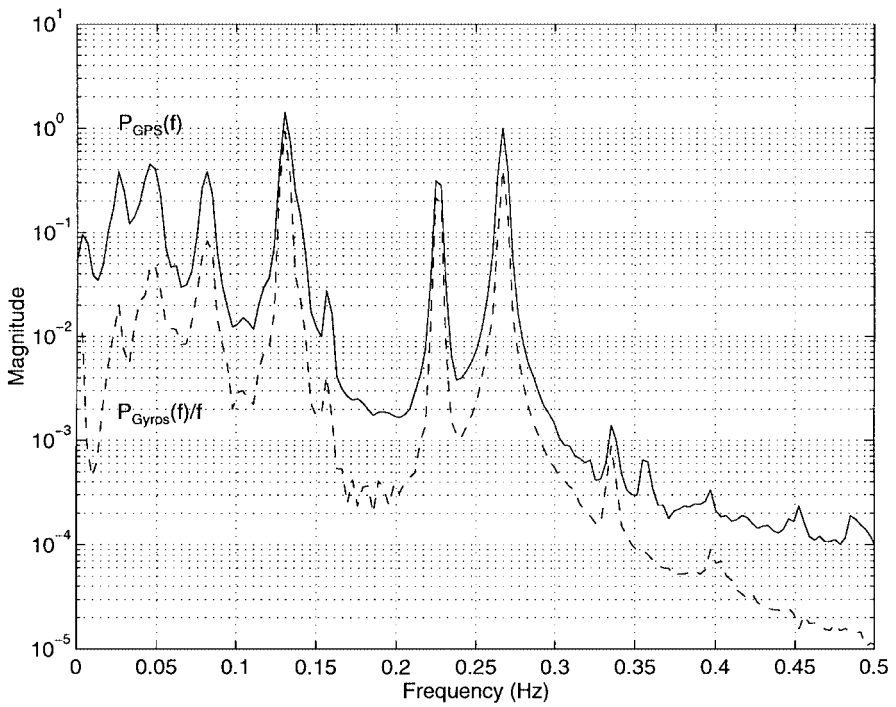

Fig. 8 Comparison of GPS- and gyro-based spectra.

accurate to resolve many of the modes of vibration. The following sections show how this sensor information can be used to simultaneously control the attitude and vibration of the test structure.

C. Pulse Disturbance Rejection

The first test of the GPS-based feedback controller demonstrates the system response to a distributed-pulse disturbance. For this test, a pulse disturbance was chosen that imparts zero total angular momentum to the entire structure, preventing undesirable large rigid-body horizontal axis rotations for the open-loop case. The zero angular momentum pulse chosen was a 1-s firing of the four thrusters shown in Fig. 9. The pulse tends to positively rotate the center section (q_5 increasing) and negatively rotate the end section (q_8 decreasing). Both

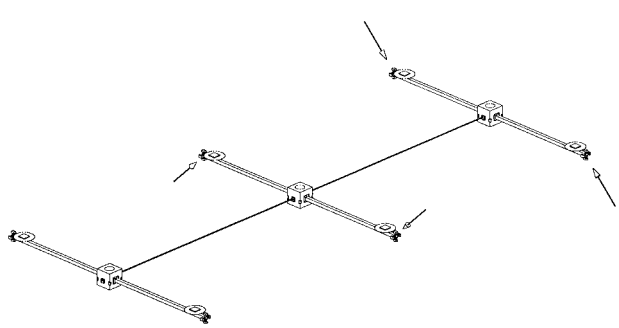

Fig. 9 Pulse thrusters showing direction and relative magnitude.

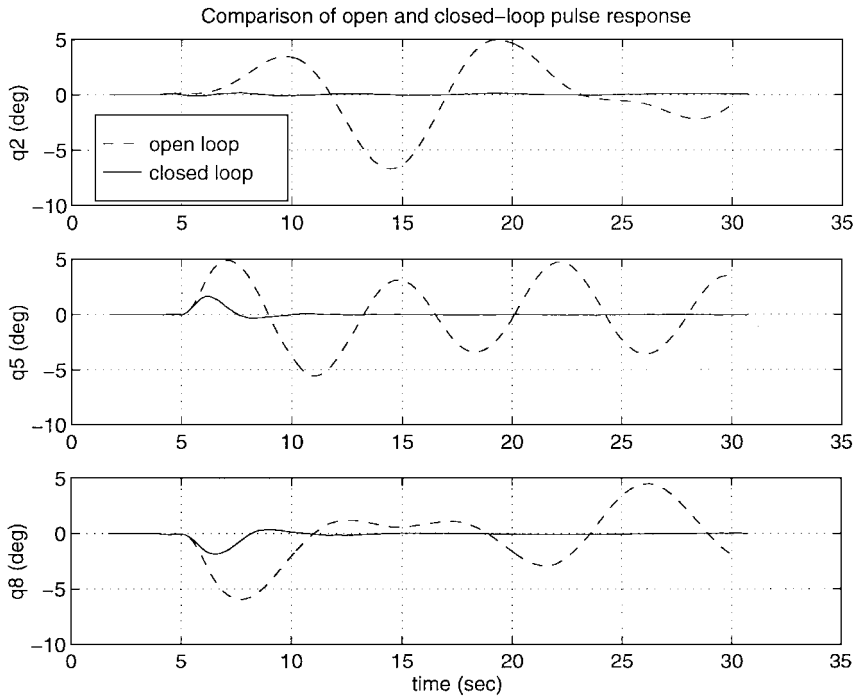

Fig. 10 Open- and closed-loop pulse response.

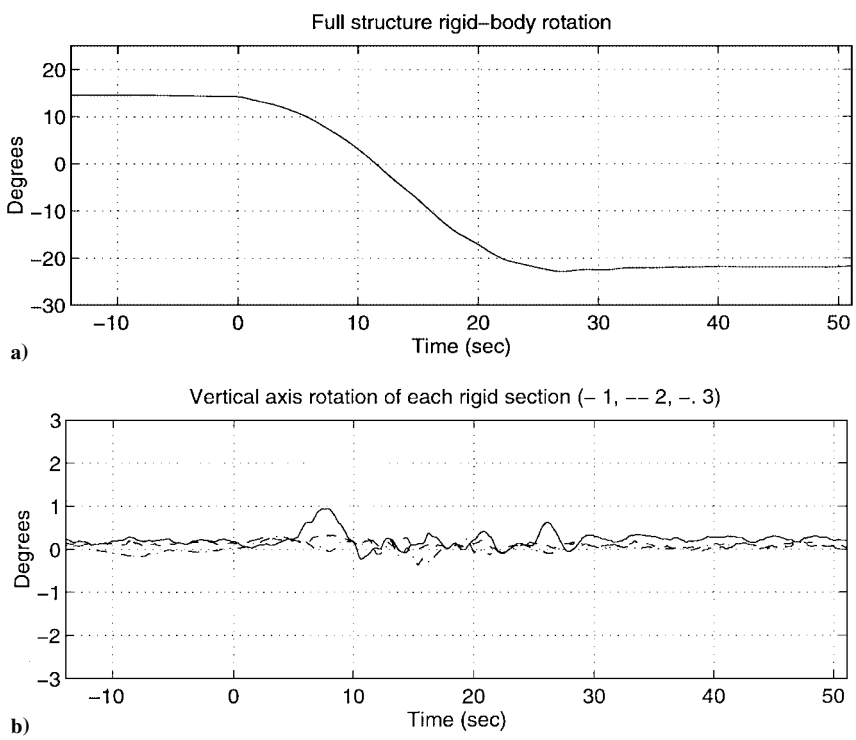

Fig. 11 Slew maneuver control with vibration control.

open- and closed-loop system responses are compared to show the performance of the active vibration control.

Figure 10 illustrates the open- and closed-loop time responses of the longitudinal twist (LT) angles. The pulse was delivered at approximately 5 s on the plot. For the open-loop test, the pulse excited the LT angles to essentially steady harmonic oscillations that are approximately 10 deg peak-to-peak. These open-loop oscillations persisted with no perceptible damping for the remaining 25 s of the test. The plots show that q_5 immediately moved in the positive direction and q_8 in the negative direction after the pulse, as expected given the torques induced by the pulse. Whereas q_5 and q_8 responded immediately, the motion of q_2 lagged by approximately 2 s. This lag also was expected because, although the thruster pulse affects q_5 and q_8 directly, q_2 is only influenced indirectly through the elastic beam.

When the same pulse was applied to the system with the control loop closed, the system returned to the initial configuration within 3 s of the end of the pulse. The results in Fig. 10 show that q_5 and q_8 again respond immediately to the pulse but the peak amplitude is only about one-third the magnitude of the first open-loop oscillation peak. Note that the motion of q_2 is not perceptible on the same graph scale. This illustrates a powerful benefit of the multi-input/multi-output control design because the distributed disturbance is essentially eliminated before it can even propagate to the third block.

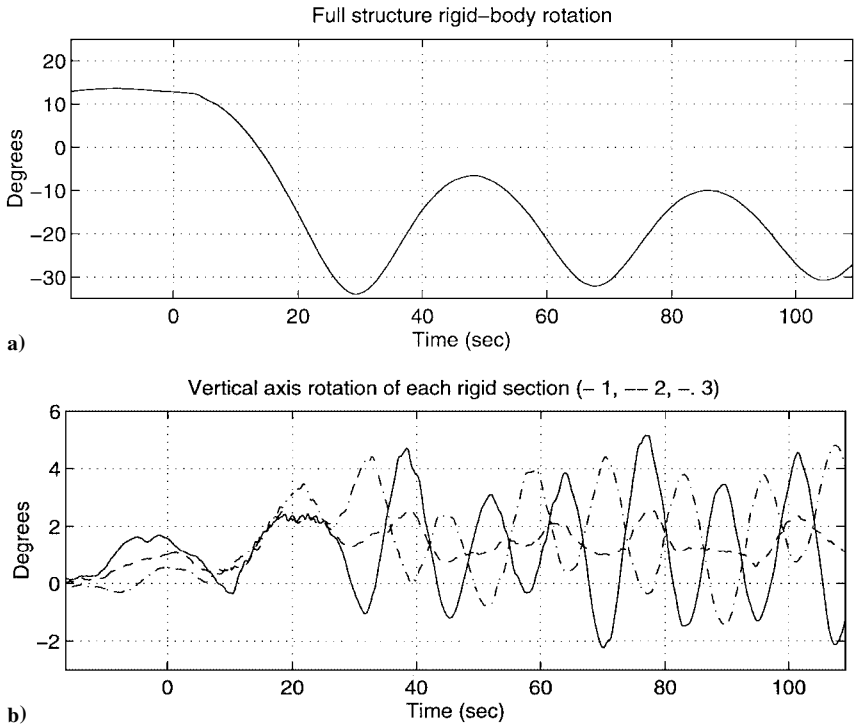

Fig. 12 Slew maneuver control with no vibration control.

D. Slew Maneuver with Vibration Suppression

The last experiment demonstrates the ability of the GPS-based control system to perform a slew maneuver. In this experiment, the controller performs a rigid-body rotation of the structure while still minimizing internal vibrations that might be excited during the maneuver. This corresponds to an ideal test of the overall system performance because it tests the ability of

1) the GPS system to sense overall system orientation,

2) the controller to successfully execute a large-scale platform orientation maneuver, and

3) the GPS to sense, and the controller to suppress, internal elastic vibrations of the structure during the slew maneuver.

To perform the test, the entire structure was rotated 14 deg in the horizontal plane and left at rest. At time zero, a command for −22 deg rigid body was issued to the control system. The controller completed the rotation maneuver within 30 s after the control initiation. Note that this slew maneuver is quite fast (>70 deg/min) given the limited thruster force available and the large rotation inertia associated with the motion.

Figure 11 shows the time response plots of the rigid-body rotation angle (q_{10}) before and after the commanded slew. Figure 11a shows the estimated slew angle, which settles to within 0.5 deg of the desired value, as measured by GPS. Figure 11b shows the relative vertical axis rotations of each of the rigid sections of the structure (q_2, q_5, and q_8). Recall that the slew is in the horizontal plane, and so, these angles should be zero. However, the thrusting forces imparted on the structure to perform the slew maneuver introduce disturbances that excite the structural vibrations. These plots clearly illustrate that the GPS-based control system is capable of eliminating the internal vibrations (to within 1 deg) during a slew maneuver.

To illustrate the importance of this vibration suppression during a controlled slew, a similar maneuver was performed on the structure without vibration control. A low-bandwidth controller was designed to damp the rigid-body pole to approximately the same level as shown in Fig. 6 without changing the vibration-mode poles (high-frequency closed-loop system poles are the same as the open-loop ones). For this test, the same 14- to −22-deg motion was commanded. As shown in Fig. 12, the control performance is much worse without the vibration control. In fact, Fig. 12b shows that significant internal vibrations are excited by the slew actuation. Also, the ability of the controller to settle to the desired final rigid-body angle is degraded without vibration suppression, as illustrated by the large-scale harmonic motion about the desired final orientation in Fig. 12a.

VII. Conclusions

A comprehensive discussion of the control system that was developed for a flexible structure using a carrier-phase GPS sensor is presented. This includes a detailed analysis of the structural model, the full-state feedback regulator, and the real-time nonlinear EKF. The results of several new experiments also are presented that clearly demonstrate the excellent static (≤0.1-deg error) and dynamic performance of the GPS sensor. The measured spectra show that the carrier-phase GPS techniques are sufficiently accurate to resolve many of the modes of vibration. Furthermore, several feedback control experiments are used to show that the sensor provides an accurate and robust measure of the structural deformations. These experiments culminate in a fast slew maneuver under feedback control that provides a clear demonstration of the application of carrier-phase GPS for both alignment and vibration control. These results mark one of the most complex applications of carrier-phase GPS as a sensor for real-time control that has ever been demonstrated.

Acknowledgments

This work was sponsored by NASA under Grant NAS8-39225. The authors thank Mladen Chargin and Roy Hampton at NASA Ames Research Center for access to and help with MSC/NASTRAN. Thanks also is given to Trimble Navigation for the GPS hardware. This research would not have been possible without the assistance and insights of K. R. Zimmerman, Konstantin Gromov, H. S. Cobb, and C. E. Cohen. Thanks also is given to the Hansen Experimental Physics Laboratory at Stanford for the space to perform these experiments.

References

[1] Parkinson, B. W., "Origins, Evolution, and Future of Satellite Navigation," *Journal of Guidance, Control, and Dynamics*, Vol. 20, No. 1, 1997, pp. 11–25.

[2] Kruczynski, L. R., Li, P. C., Evans, A. G., and Hermann, B. R., "Using GPS to Determine Vehicle Attitude: USS Yorktown Test Results," Inst. of Navigation, International Technical Meeting of the Satellite Div., Colorado Springs, CO, Sept. 1989, pp. 163–171.

[3]van Graas, F., and Braasch, M., "GPS Interferometric Attitude and Heading Determination: Initial Flight Test Results," *Navigation: Journal of the Institute of Navigation*, Vol. 38, No. 4, 1991, pp. 359–378.

[4]Cohen, C. E., "Attitude Determination Using GPS," Ph.D. Thesis, Dept. of Aeronautics and Astronautics, Stanford Univ., Stanford, CA, Dec. 1992.

[5]Lightsey, E. G., Cohen, C. E., and Parkinson, B. W., "Application of GPS Attitude Determination to Gravity Gradient Stabilized Spacecraft," *Proceedings of the AIAA Guidance, Navigation, and Control Conference*, AIAA, Washington, DC, 1993.

[6]Conway, A. R., "Autonomous Control of a Model Helicopter Using Carrier Phase GPS," Ph.D. Thesis, Dept. of Electrical Engineering, Stanford Univ., Stanford, CA, March 1995.

[7]O'Connor, M. L., Elkaim, G. H., and Parkinson, B. W., "Carrier-Phase DGPS for Closed-Loop Control of Farm and Construction Vehicles," *Navigation: Journal of the Institute of Navigation*, Vo. 43, No. 2, 1996, pp. 167–178.

[8]Axelrad, P., and Ward, L. M., "Spacecraft Attitude Estimation Using the Global Positioning System: Methodology and Results for RADCAL," *Journal of Guidance, Control, and Dynamics*, Vol. 19, No. 6, 1996, pp. 1201–1209.

[9]Parkinson, B. W., Spilker, J. J., Axelrad, P., and Enge, P., *GPS: Theory and Applications*, AIAA, Washington, DC, 1996.

[10]Cohen, C. E., McNally, B. D., and Parkinson, B. W., "Flight Tests of Attitude Determination Using GPS Compared Against an Inertial Navigation Unit," *Nagivation: Journal of the Institute of Navigation*, Vol. 41, No. 1, 1994, pp. 83–97.

[11]Zimmerman, K. R., "Experiments in the Use of the Global Positioning System for Space Vehicle Rendezvous," Ph.D. Thesis, Electrical Engineering Dept., Stanford Univ., Stanford, CA, Dec. 1996.

[12]Sparks, D. W., Jr., and Juang, J. N., "Survey of Experiments and Experimental Facilities for Control of Flexible Structures," *Journal of Guidance, Control, and Dynamics*, Vol. 15, No. 4, 1992, pp. 801–816.

[13]Hyland, D. C., Junkins, J. L., and Longman, R. W., "Active Control Technology for Large Space Structures," *Journal of Guidance, Control, and Dynamics*, Vol. 16, No. 5, 1993, pp. 801–821.

[14]Grocott, S., How, J. P., Miller, D., MacMartin, D., and Liu, K., "Robust Control Design and Implementation on the Middeck Active Control Experiment (MACE)," *Journal of Guidance, Control, and Dynamics*, Vol. 17, No. 6, 1994, pp. 1163–1170.

[15]Teague, E. H., and Parkinson, B. W., *Translation, Rotation, and Vibration Control of Large Space Structures Using Self-Differential GPS (SDGPS)*, Vol. 81, Advances in the Astronautical Sciences, Guidance and Control, American Astronautical Society, Springfield, VA, 1993, pp. 93–101.

[16]Teague, E. H., "Flexible Structure Estimation and Control Using the Global Positioning System," Ph.D. Thesis, Dept. of Aeronautics and Astronautics, Stanford Univ., Stanford, CA, May 1997.

[17]Teague, E. H., How, J. P., and Parkinson, B. W., "Carrier Differential GPS for Real-Time Control of Large Flexible Structures," *Navigation: Journal of the Institute of Navigation*, Vol. 44, No. 2, 1997, pp. 215–229.

[18]Lightsey, E. G., and Parkinson, B. W., "GPS Based Attitude Determination on Nonaligned Antenna Arrays," Inst. of Navigation, GPS-96 Conf., Kansas City, MO, Sept. 1996, pp. 1081–1090.

[19]Cohen, C. E., and Parkinson, B. W., *Mitigating Multipath Error in GPS Based Attitude Determination*, Vol. 74, Advances in the Astronautical Sciences, Guidance and Control, American Astronautical Society, Springfield, VA, 1991.

[20]Axelrad, P., Comp, C. J., and MacDoran, P. F., "SNR Based Multipath Error Correction for GPS Differential Phase," *IEEE Transactions on Aerospace and Electronics Systems*, Vol. 32, No. 2, 1997, pp. 650–660.

[21]Lawrence, D., Cobb, H. S., Cohen, C., Christie, J., Powell, J. D., and Parkinson, B., "Maintaining GPS Positioning in Steep Turns Using Two Antennas," Inst. of Navigation, GPS-95 Conf., Palm Springs, CA, Sept. 1995, pp. 1451–1459.

[22]Bauer, F. H., Lightsey, E. G., McCullough, J. M., O'Donnell, J., and Schnurrk, R., "GPS Attitude Determination Flyer GADFLY: A Space Qualified GPS Attitude Receiver on the SSTI-Lewis Spacecraft," Inst. of Navigation, GPS-95 Conf., Palm Springs, CA, Sept. 1995, pp. 555–572.

[23]Cohen, C. E., Cobb, H. S., Lawrence, D. G., Pervan, B. S., Powell, J. D., Parkinson, B. W., Aubrey, G. J., Loewe, W., Ormiston, D., McNally, B. D., Kaufmann, D. N., Wullschleger, V., and R. J. Swinder, Jr., "Autolanding a 737 Using GPS Integrity Beacons," *Navigation: Journal of the Institute of Navigation*, Vol. 42, No. 3, 1995, pp. 467–486.

[24]O'Connor, M. L., Bell, T., Elkaim, G., and Parkinson, B. W., "Real-Time CDGPS Initialization for Land Vehicles Using a Single Pseudolite," Inst. of Navigation, National Technical Meeting, Santa Monica, CA, Jan. 1997.

[25]Franklin, G. F., Powell, J. D., and Workman, M., *Digital Control of Dynamic Systems*, 2nd ed., Series in Electrical and Computer Engineering: Control Engineering, Addison–Wesley, Reading, MA, 1990, pp. 135–155.

[26]Gelb, A., *Applied Optimal Estimation*, MIT Press, Cambridge, MA, 1974, pp. 186–192.

[27]Kwakernaak, H., and Sivan, R., *Linear Optimal Control Systems*, Wiley-Interscience, New York, 1972, p. 211.